High Torque Bearingless Flux-Switching Slice Drive

Karlo RADMAN*, Wolfgang GRUBER**, Neven BULIĆ***

*Linz Center of Mechatronics GmbH
Altenberger Str. 69, 4040 Linz, Austria
E-mail: karlo.radman@lcm.at
**Institute for Electrical Drives and Power Electronics, Johannes Kepler University Linz
Altenberger Str. 69, 4040 Linz, Austria
***Department of Automation and Electronics, Faculty of Engineering, University of Rijeka
Vukovarska 58, 51000 Rijeka, Croatia

Abstract

This paper presents the development of a bearingless flux-switching slice drive. Belonging to the bearingless drive family, all active and passive suspension forces are generated in the same radial plane and with the same electromechanical components which generate the motor torque. This research had the goal of improving the torque capabilities of the drive while still maintaining adequate passive slice-rotor stabilization. Optimization goals included the increment of the air gap and the motor torque increase, two opposing demands. A working prototype was built from the optimized simulation model. The prototype's torque and suspension force performances were measured and compared to the FEM simulation results. Additionally, a new control model is proposed for the bearing force generation.

Keywords : Bearingless, Flux-Switching, Slice Drive, FSPM, Optimization

1. Introduction

A high torque bearingless flux-switching slice drive was researched and developed in continuation with the previous work (Radman, et. al., 2014a, 2014b) done in the field of bearingless flux-switching drives BLFSD. The relative term high torque denotes that the drive was designed for maximized torque generation while complying with the set geometrical and operational requirements. These requirements include a motor outer diameter smaller than 300 mm and an air gap not smaller than 4 mm. The drive geometry was optimized using 3D FEM simulations (Radman, et. al., 2015). Variable geometry parameters include the motor height, permanent magnet (PM) size and stator teeth shape.

The first chapter describes the topology and working principles of the torque and bearing force generation. Secondly, a new simplified control model is proposed for the specific BLFSD bearing system. The succeeding chapters present the optimization results and the prototype construction. Finally the measurements are compared to the FEM simulations.

2. Flux-switching permanent magnet motor

The flux switching permanent magnet motor (FSPM) is a permanent magnet (PM) synchronous motor with a topology that has the PM field and armature producing components on the stator side. The salient stator has a field producing PM in the middle of each tooth and an armature coil wound around it, as shown in Fig 1. The rotor consists only of a salient ring made from laminated iron. The rotation alters the PM flux path due to the angle dependent reluctance, and hence a sinusoidal flux change can be observed inside the armature coils. Figure 2 depicts the influence of the rotor angle on the PM flux path. The detailed stator geometry and parameters are presented in Fig. 3.

The topology works with different rotor and stator teeth numbers (Chen and Zhu, 2010a), with the 12 stator teeth and 10 rotor teeth combination being the optimal for the bearingless control (Gruber, et. al., 2014). As the field is switched a whole period with every tooth pitch rotation, each rotor tooth corresponds to a pole pair. Opposing stator coils can be connected in phase due to rotor symmetry. For a topology with 12 stator teeth that will lead to 6 phases out of which three will be used for torque generation, making the motor a consecutive pole wound FSPM (Chen and Zhu, 2010b).

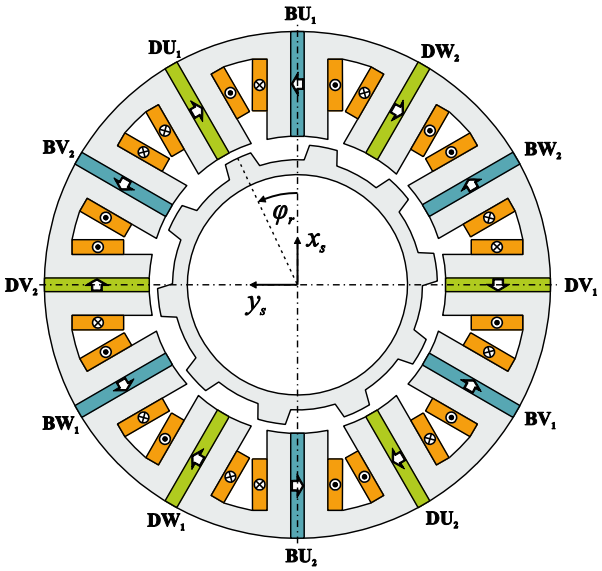

Fig. 1 The BLFSD topology. Segments marked with D belong to the drive, torque producing phases and the segments marked with B to the bearing phases. Arrows represent PM field orientation.

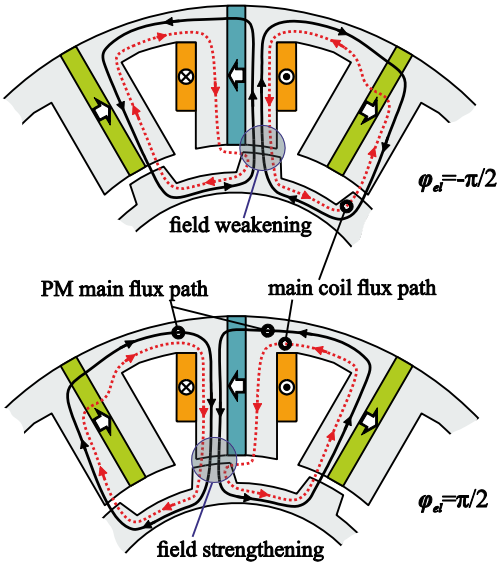

Fig. 2 The flux-switching principle. Angle dependent rotor reluctance alters the PM flux path. The coil is energized as depicted and exerts a field weakening or strengthening depending on the angle.

2.1 Bearingless flux-switching slice drive

The drive belongs to the family of bearingless slice drives, having three degrees of freedom (DOF) passively stabilized by reluctance forces (Salazar, et. al., 2000). Passive stabilization implies that the forces counteract the rotor movement from the drive's center aligned operational point. These DOF include the rotor displacement along the drive z-axis and the rotor tilt around the x and y-axis (Fig. 1). To achieve a stabilizing torque that counters the rotor tilting, the rotor has to be slice shaped, having the rotor diameter a few times greater than its height (Schöb and Barletta, 1996), (Gruber, 2013). The axial stabilizing force and tilt stabilizing torque are geometry and PM material depended and have to be assessed during the geometry optimization.

The remaining DOF are the rotor z-axis rotation controlled by the motor torque phases and the x-and y-axis rotor displacement controlled by the bearing phases. The bearing force phases have to counteract the passive radial destabilizing forces, the rotation unbalance and the gyroscopic effects.

3. Bearing force generation

The bearing forces are generated in the same plane as the motor torque. Each winding current exerts a radial and tangential force component on the rotor. If the opposing coils (phases DU, DV and DW in Fig. 1) are connected in such a manner that the coil's normal force components are pointing in opposing direction, only the tangential force components are left and a torque is exerted on the rotor, as shown in Fig. 4 for a single DC energized phase.

An inverse connection of opposing coils (phases BU, BV and BW in Fig. 1) will exert a sum of the normal and tangential forces of both phase coils as shown in Fig. 4. In this configuration the quadratic terms cancel-out and a linearly current depended bearing force is achieved (Gruber, 2014). This phases are not generating torque, and we can assume a decoupled torque and force generation in the not saturated operating cases. The first case is the start of rotor levitation when the highest bearing currents are needed for liftoff and no torque is produced. The second case is while motor torque is generated and minimal bearing currents are needed as the negative destabilizing radial force is the smallest in the centered position.

3.1 Force control matrix

Each bearing phase generates a sinusoidal angle dependent force on the rotor as shown in Fig. 4. If the higher

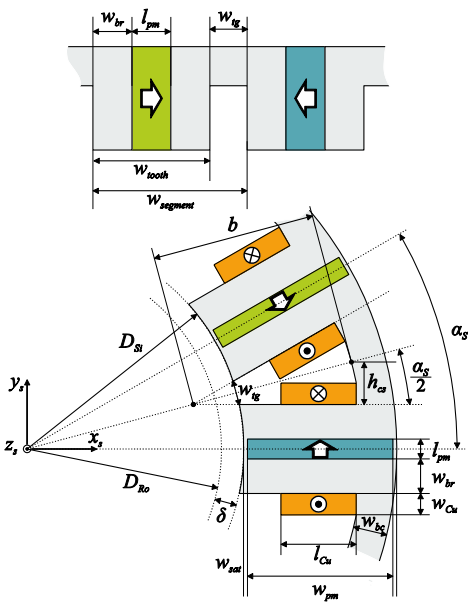

Fig. 3 Simplified stator tooth model (top). All stator geometry parameters (down)

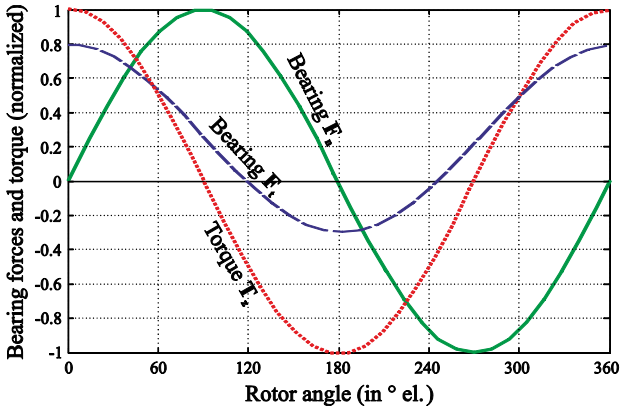

Fig. 4 Normalized torque and force generation over the rotor electric angle. The torque is the result of a motor phase (DU, DV or DW in Fig. 1) energised by DC current. The forces are the result of a DC energised bearing phase (BU, BV or BW in Fig. 1). The tangential force has a offset which is lenearly current dependent. Bearing phases have inversly connected windings (e.g. BU_1 and BU_2 in Fig. 1)

harmonics are relatively small compared the first harmonic, the force equations can be expressed as

$$F_n^m(i_{m,}\varphi_{el}) = A_n \cdot \sin(\varphi_{el}) \cdot i_{bm} \tag{1}$$

$$F_t^m(i_{m,}\varphi_{el}) = (D_t + A_t \cdot \cos(\varphi_{el})) \cdot i_{bm} \ , \tag{2}$$

where F_n denotes the normal and F_t the tangential force component relative to the phase m axis. I_{bm} is the respective bearing phase current and φ_{el} the electrical rotor angle. Constants A_n and A_t represent the characteristic amplitudes and D_t the mean part of the tangential force. For a three-phase bearing system the stator fixed normal F_x and tangential F_y force (x_s- and y_s-axis direction in Fig. 1) can be expressed as

$$\begin{bmatrix} F_x \\ F_y \\ 0 \end{bmatrix} = \boldsymbol{T_m} \cdot \begin{bmatrix} i_{b1} \\ i_{b2} \\ i_{b3} \end{bmatrix} \ , \tag{3}$$

where T_m is the current-force relation matrix. The last row in the force matrix is the star connection constrain, defining that the sum of all three currents is zero. The T_m matrix consists of a normal and tangential force contributions of all three bearing phases shifted mechanically and electrically by 120° and projected on the stator fixed xy frame. The matrix can be normalized with the amplitude A_n from Eq. (1), producing the normalized coefficients A for the amplitude A_t and the coefficient D for the D_t constant, and the matrix T_m can be expressed as

$$\boldsymbol{T_m} = A_n \cdot \begin{bmatrix} \sin(\varphi_{el}) & -\frac{1}{2}\sin\left(\varphi_{el} - \frac{2}{3}\pi\right) - \frac{\sqrt{3}}{2}\left[D + A\cos(\varphi_{el} - \frac{2}{3}\pi)\right] & -\frac{1}{2}\sin\left(\varphi_{el} - \frac{4}{3}\pi\right) + \frac{\sqrt{3}}{2}\left[D + A\cos(\varphi_{el} - \frac{4}{3}\pi)\right] \\ D + A\cos(\varphi_{el}) & \frac{\sqrt{3}}{2}\sin\left(\varphi_{el} - \frac{2}{3}\pi\right) - \frac{1}{2}\left[D + A\cos(\varphi_{el} - \frac{2}{3}\pi)\right] & -\frac{\sqrt{3}}{2}\sin\left(\varphi_{el} - \frac{4}{3}\pi\right) - \frac{1}{2}\left[D + A\cos(\varphi_{el} - \frac{4}{3}\pi)\right] \\ 1 & 1 & 1 \end{bmatrix} \tag{4}$$

Currents, deduced from the needed bearing force, have to be sent into the bearing phases to control the rotor position. Therefore, the inverse of the T_m matrix must be computed which leads to the force to current matrix

$$\begin{bmatrix} i_{b1} \\ i_{b2} \\ i_{b3} \end{bmatrix} = \boldsymbol{T_m}^{-1} \cdot \begin{bmatrix} F_x \\ F_y \\ 0 \end{bmatrix} \ . \tag{5}$$

In the case of the BLFSD with separated torque and bearing phases a specific solution can be computed for each rotor angle as the T_m is a square 3x3 matrix.

4. Optimization

To improve the capabilities compared to the first ever built BLFSD (Radman, et. al., 2014a) a 3D FEM optimization has been carried out. The BLFSD optimization was conducted in two steps, where firstly the rotor diameter, motor height and air gap width were analyzed and secondly the stator tooth geometry (Radman, et. al., 2015). The geometry variations are within the boundaries summarized in Table 1. The parameters kept constant during the simulations are listed in Table 2.

The stator tooth optimization analyzes the influence of the width of the teeth iron and PM segments, with the stator geometry parameters marked in Fig. 3. The variations are expressed over the stator pole pitch w_{pitch} to the tooth width w_{tooth} ratio defined as

$$S = \frac{w_{pitch}}{w_{tooth}} \tag{6}$$

and the ratio of the flux collecting iron part of the tooth to the total tooth width

$$IPR = \frac{2 \cdot w_{br}}{w_{tooth}} \ . \tag{7}$$

The conventional geometry used in the FSPM drive design has the PM length l_{pm}, the iron width w_{br} and the inter teeth gap w_{tg} of equal length (Chen and Zhu, 2010a). This leads to an S of 1.33 and an IPR ratio of 0.66. A smaller S increases the teeth width, enabling more space for the iron and PM teeth elements, and thus reduces the available space for the winding. A smaller IPR value increases the magnet length inside the teeth, but reduces the flux guiding iron width w_{br} which leads to higher saturation. Iron saturation has to be avoided to preserve a linear force-current correlation.

4.1 Motor size optimization

The first optimization goal was to increase the air gap while not lowering the torque and suspension performance. An air gap bigger than 3 mm is needed to accommodate a separation chamber between the rotor and stator. To counteract the air gap increase, the motor height was increased. The maximal height is limited by the passive tilt stability, which is restricted to slice shaped rotors. Figures 5 and 6 show the tilt stabilizing torque for a 1° tilted rotor with varying air gap, motor height and rotor diameter. A height dependent maximum in passive tilt stability is achievable, above which the tilt torque declines with the increasing height until a negative destabilizing torque is present, rendering bearingless operation impossible.

Motor characteristics including the axial stabilizing force, the motor torque and bearing force capabilities increase with the motor height. The passive radial destabilizing force also increases with the height but with a faster rate than the active bearing force as presented in Fig. 7. This can lead to a design with insufficient bearing force to liftoff the rotor when it is maximally displaced from the center. Figure 8 shows the torque dependency on the air gap and height.

Table 1 Optimization geometry variable boundaries

Motor size optimization		
Variable	Min [mm]	Max [mm]
Rotor outer diameter D_{Ro}	150	200
Motor height h	10	40
Air gap δ	3	5
Motor outer diameter[a] D_{So}	266	320
Stator tooth optimization		
Variable	Min	Max
S	1.2	1.4
IPR	0.533	0.8

[a.] Depending on air gap and rotor outer diameter

Table 2 Motor constant dimension

Motor size simulations	
Parameter	Value
IPR[a]	1.26
S[a]	0.73
PM radial length[b] w_{pm} [mm]	54
Stator back iron[b] w_{bc} [mm]	14
Stator tooth simulations	
Parameter	Value
Rotor diameter D_{Ro} [mm]	170
Motor height h [mm]	30
Motor outer diameter D_{So} [mm]	288
Air gap δ [mm]	4

[a.] Same as in the first built BLFSD (Radman, et. al., 2014a)

[b.] Also valid for the stator teeth geometry simulation

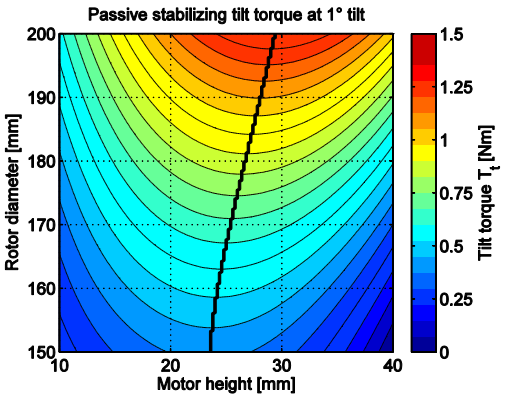

Fig. 5 Passive tilt torque over the rotor diameter and motor height, the black line denotes the maximum. Air gap, δ is 4 mm.

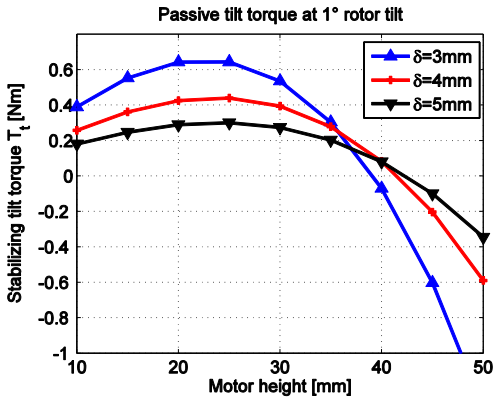

Fig. 6 Passive tilt torque for a 1° rotor tilt for a varying air gap and motor height. Geometries with negative tilt torque solutions are unstable

4.2 Stator teeth optimization

The second optimization cycle analyzes the same bearingless drive characteristics as the previous, additionally including the current density in the coils as it is affected by the ratio S and the torque ripple expressed by the total harmonic distortion THD. The simulations were done for the variable range listed in Table 1 and geometry values listed in Table 2. The bearing force dependency on the variables *S* and *IPR* is shown in Fig. 9. The torque dependency is presented in Fig. 10. Both show an increase with the reduction of *S* which is due to the increase of the PM volume.

The design objectives include an axial displacement of less than 1 mm, which means that the passive stabilizing axial force per milimeter has to be greater than the rotor weight. The stabilizing tilt torque has to be greater than 0.7 Nm and the current density less than 6 A/mm^2 for a motor torque of 8 Nm. Liftoff capability has to be possible for a rotor displacement of at least 0.8 mm while the lamination stack is not allowed to be saturated under the maximal MMF of 3 kA. The result of the simulations are presented together by mentioned objectives in Fig 11.

The remaining white area in Fig. 11 holds the preferable solution that meets all requirements. Solution marked with the dot P in Fig. 11 is the conventional geometry with an *S* of 1.33 and *IPR* of 0.66. This, corresponds to a stator tooth with evenly spaced flux collecting iron w_{br}, permanent magnets l_{pm} and an inter teeth gap w_{tg}.

The first optimization cycle showed that the motor torque is greatly influenced by the air gap width. A compromise was made by choosing an air gap of 4 mm. For a 4 mm air gap, the maximal tilting stabilization torque is at a motor height of 25mm, as shown in Fig. 6. From the second optimization cycle the parameters S and IPR were chosen to be 1.33 and 0.66 respectively. The rotor diameter was set at 150 mm for the development of the prototype.

The rotor tooth geometry was based on available optimization data for conventional FSPM machines (Hua, et. al., 2007) and was not altered in the simulations.

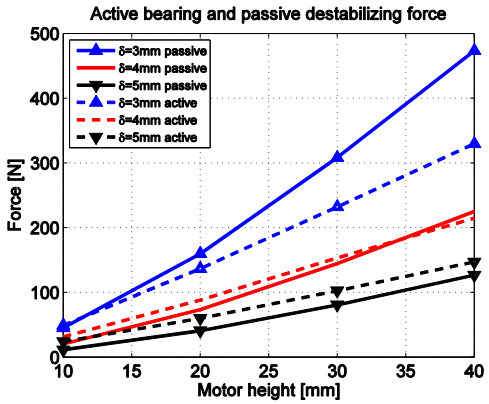

Fig. 7 Active bearing force at 3000AT and passive destabilizing radial force at 1mm displacement. A higher active force is needed for rotor liftoff.

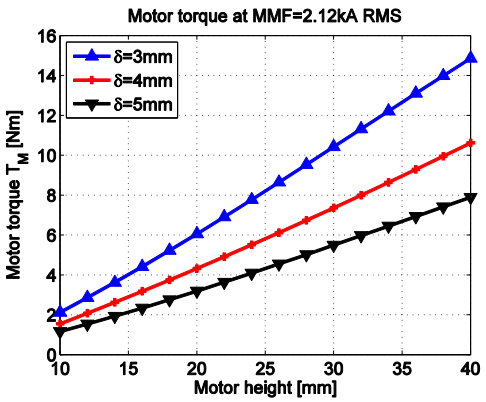

Fig. 8 Motor torque at 3000 AT peak (2.12 AT RMS). Between a 3 and 4 mm air gap the torque drops by 30% and between 4 and 5 mm by additional 25%.

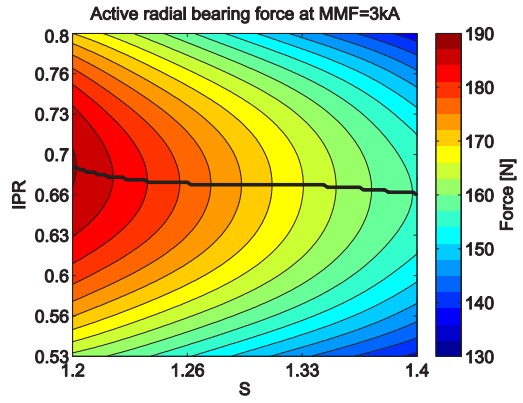

Fig. 9 Active bearing force for a varying stator tooth geometrie. An IPR ratio dependent maximum is marked with the thick line

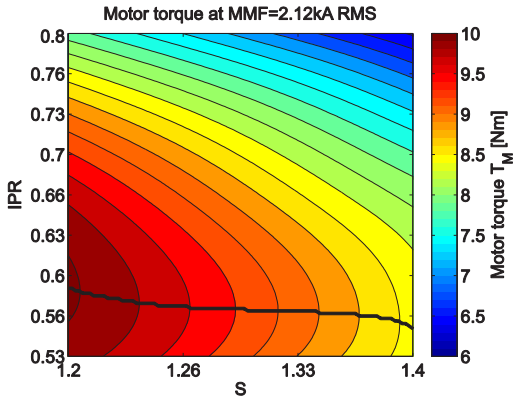

Fig. 10 Motor torque for a varying stator tooth geometrie. An IPR ratio dependent maximum is marked with the thick line

7. Prototype construction and measurement

A prototype drive was built from the optimization results to assess the performance and the control system feasibility. Geometry parameters used to build the BLFSD are listed in Table 3. The finished drive is shown in Fig. 12. The drive was put into operation with a power electronic consisting of two three-phase half bridge inverters, one for the motor torque and the second for the bearing force generation.

7.1 Measurement

The measurements were done for the motor and bearing phases separately. The simulation results and measurements are listed in Table 4. For the motor phases the rotor was connected to a load machine. The measured induced voltage is presented in Fig. 13. The under load drive power for up to 6 Nm is shown in Fig 14 for a rotational speed of 600 rpm. Due to the high phase inductances the power factor is relatively low. The phase inductance and coil turn number are high due to the need for a linked flux in the range of 2.5k AT to generate sufficient torque with the 4 mm air gap.

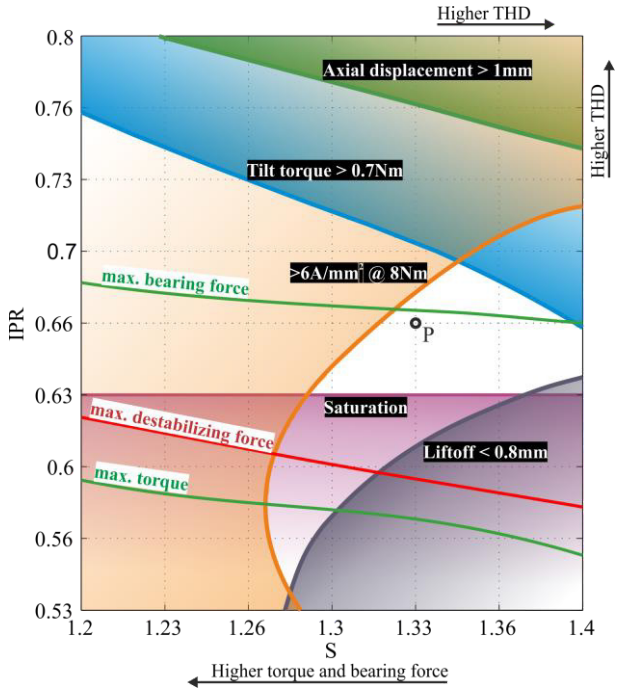

Fig. 11 Stator teeth geometry guidelines. Colored areas represent variations that don't meet the requirements.

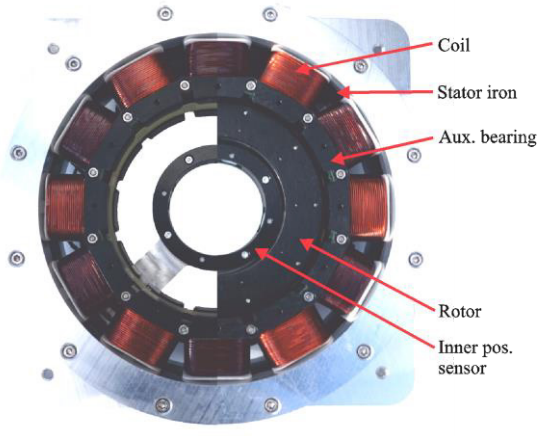

Fig. 12 The prototype BLFSD assembly. Half of the rotor is removed in the picture for clarification. The drive consists of the stator coils with separate winding numbers for torque and force generation, stator embedded NdFeB PM, laminated iron for the rotor and stator and a composite material auxiliary bearing to limit the rotor radial displacement to 2 mm.

Table 3 BLFSD prototype parameters

Parameter	Value
IPR	1.26
S	0.73
Rotor outer diameter D_{Ro} [mm]	150
Rotor inner diameter D_{Ri} [mm]	110
Motor outer diameter[a] D_{So} [mm]	270
Motor height h [mm]	25
Air gap δ [mm]	4
PM radial length w_{pm} [mm]	54.8
Stator back iron w_{bc} [mm]	14
PM magnet material	N35H
Laminated sheet material	M350-50A
Motor coil no. of turns	115
Bearing coil no. of turns	120

Table 4 Motor simulated and measured performance

Factor	Simulation	Measurement	Unit
Radial negative stiffness	-118	-113	N/mm
Axial stiffness	11.8	11.5	N/mm
Tilt stiffness	30.5	-	Nm/rad
Bearing constant	9.81	9.31	N/A
Torque constant	0.615	0.598	Nm/Arms
Current limit	11		Arms
Supply voltage	320		Vdc

The rotor was connected to a 3 DOF force measurement transducer and the drive was put on an adjustable xyz-table, as pictured in Fig.15. Passive and bearing capabilities were measured and the data is compared to the simulation results in Fig. 16, Fig.17 and Fig. 18. The error from the expected simulation results is in the relatively close range of -5%. The bearing force shows saturation above 10A per phase (2400 AT) as seen in Fig. 18. The passive tilt torque was not measured on the built drive.

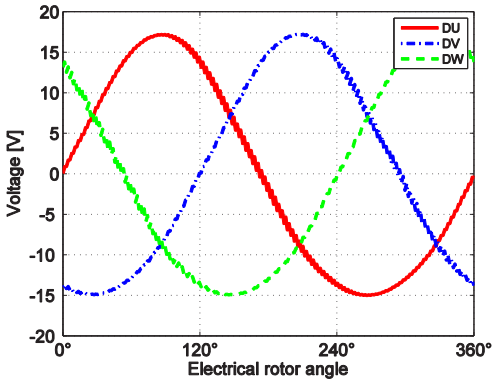

Fig. 13 Measured induced back EMF at 500 rpm. A second harmonic can be seen in the waveform.

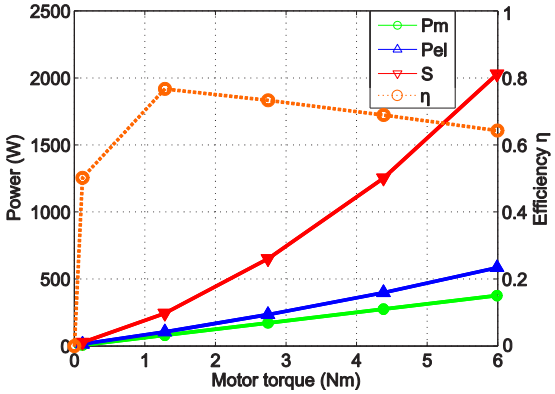

Fig. 14 Measured motor, real and complex power at 600 rpm with additionally plotted motor efficiency. The power factor at 6 Nm is around 0,28.

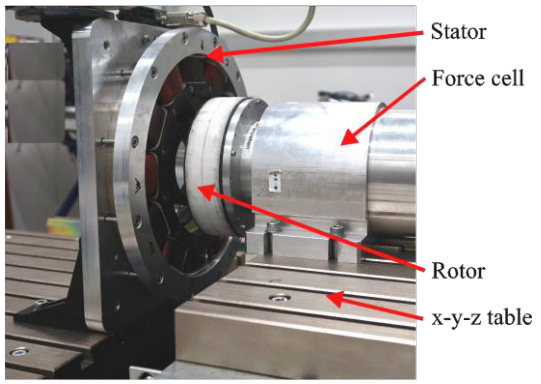

Fig. 15 Passive and active force measurement. The rotor is mounted on the force transducer and moved axially and radially relative to the stator

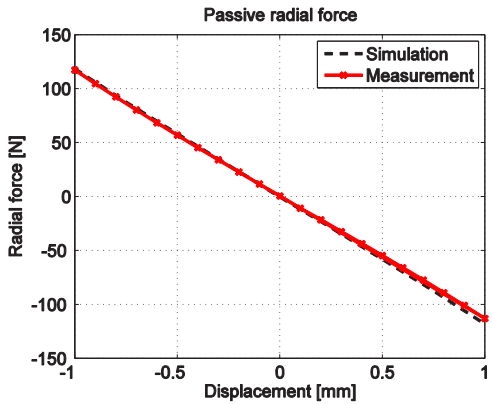

Fig. 16 Simulated and measured passive radial force along the stator x_s axis.

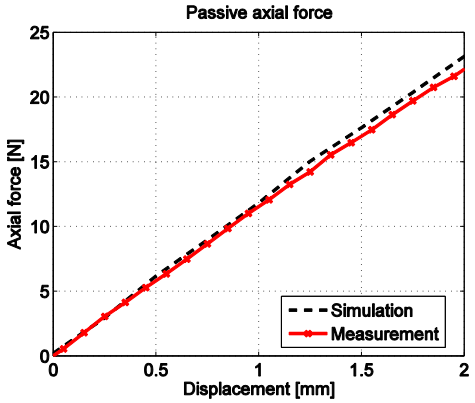

Fig. 17 Simulated and measured passive axial stabilizing force along the stator z_s axis.

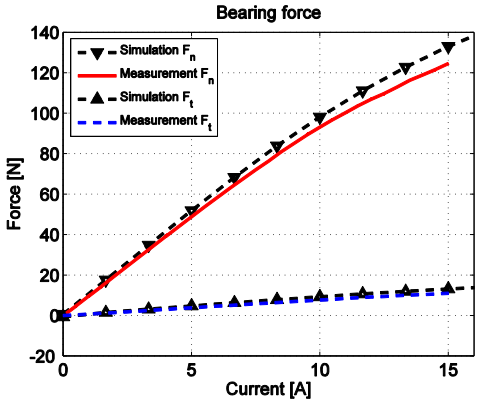

Fig. 18 Simulated and measured active radial bearing force of the bearing phase BU. The tangential is along the stator y_s axis and normal force along the stator x_s axis.

9. Conclusion

This paper presented the development of an improved BLFSD. The BLFSD has the benefit of a magnet free rotor compared to other synchronous bearingless slice drives. The built prototype proved the principle of operation of the topology and the implemented control system. With a deviation below 5% the 3D FEM simulation have been proven to give an accurate representation of the expected drive performances. This research will be further expanded by the optimization of the rotor geometry and windings. Additionally, the power factor can be improved by reducing the number of turns per torque phase and usage of an inverter with a higher output current.

Acknowledgment

Parts of this work were supported by the Linz Center of Mechatronics (LCM) GmbH, a K2-centre of the COMET program of the Austrian Government. The authors thank the Austrian and Upper Austrian Government for their support.

References

Chen, J.T.; Zhu, Z.Q., Winding Configurations and Optimal Stator and Rotor Pole Combination of Flux-Switching PM Brushless AC Machines, IEEE Transactions on the Energy Conversion (2010a), Vol.25, No.2, pp.293-302.

Chen, J.T.; Zhu, Z.Q., Comparison of All- and Alternate-Poles-Wound Flux-Switching PM Machines Having Different Stator and Rotor Pole Numbers, IEEE Transactions on Industry Applications (2010b), Vol.46, No.4, pp.1406-1415.

Gruber W., Schöb R., Radman K., Design of a Bearingless Flux-Switching Slice Motor, Proceedings of the International Power Electronics Conference (IPEC) (2014), pp.1691-1696.

Gruber, W., Bearingless Slice Motors: General Overview and the Special Case of Novel Magnet-Free Rotors, GMM/ETG Symposium on Innovative Small Drives and Micro-Motor Systems (2013), pp.1-6.

Radman K., Gruber W. and Bulic N., Loss Analysis of a Bearingless Flux-Switching Slice Motor, Proceedings of the 14th International Symposium on Magnetic Bearings (ISMB14) (2014a), pp.210–215.

Radman K., Gruber W. and Bulic N., Performance evaluation of a bearingless flux-switching slice motor, Proceedings of the 2014 IEEE Energy Conversion Congress and Exposition (ECCE) (2014b), pp.3811-3818.

Radman K., Gruber W. and Bulic N., Geometry optimization of a bearingless flux-switching slice motor, Proceedings of the 2015 IEEE International Electric Machines & Drives Conference (IEMDC) (2015), pp.1695-1701.

Salazar, A. Chiba, and T. Fukao. A review of developments in bearingless motors, Proceedings of the 7th International Symposium on Magnetic Bearings (ISMB) (2000), pp.335-401.

Schöb, R., Barletta, N., “Principle and Application of a Bearingless Slice Motor, Proceedings of the 5th International Symposium on Magnetic Bearings (ISMB) (1996), pp.333-338.

Hua W. Cheng M.; Zhu Z.Q.; Howe D., Analysis and Optimization of Back-EMF Waveform of a Novel Flux-Switching Permanent Magnet Motor, Proceedings of the 2007 IEEE International Electric Machines & Drives Conference (IEMDC) (2007), pp.1025-1030.